



A 3D-bioprinted scaffold with doxycycline-controlled BMP2-expressing cells for inducing bone regeneration and inhibiting bacterial infection

Minqi Wang^{a,1}, Hanjun Li^{a,1}, Yiqi Yang^a, Kai Yuan^a, Feng Zhou^a, Haibei Liu^b, Qinghui Zhou^b, Shengbing Yang^{a,*}, Tingting Tang^{a,*}

^a Shanghai Key Laboratory of Orthopaedic Implants, Department of Orthopaedic Surgery, Shanghai Ninth People's Hospital, Shanghai Jiao Tong University, School of Medicine, Shanghai, 200011, China

^b Shanghai Graphic Design Information Co. Ltd, Shanghai, 200011, China

ARTICLE INFO

Keywords:

3D bioprinting
Genetic engineering
Bone repair
Antibacterial activity
Infectious bone defect

ABSTRACT

Large bone defects face a high risk of pathogen exposure due to open wounds, which leads to high infection rates and delayed bone union. To promote successful repair of infectious bone defects, fabrication of a scaffold with dual functions of osteo-induction and bacterial inhibition is required. This study describes creation of an engineered progenitor cell line (C3H10T1/2) capable of doxycycline (DOX)-mediated release of bone morphogenetic protein-2 (BMP2). Three-dimensional bioprinting technology enabled creation of scaffolds, comprising polycaprolactone/mesoporous bioactive glass/DOX and bioink, containing these engineered cells. *In vivo* and *in vitro* experiments confirmed that the scaffold could actively secrete BMP2 to significantly promote osteoblast differentiation and induce ectopic bone formation. Additionally, the scaffold exhibited broad-spectrum antibacterial capacity, thereby ensuring the survival of embedded engineered cells when facing high risk of infection. These findings demonstrated the efficacy of this bioprinted scaffold to release BMP2 in a controlled manner and prevent the occurrence of infection; thus, showing its potential for repairing infectious bone defects.

1. Introduction

Large bone defect can be caused by traumatic injury, bone tumor, etc., and its clinical treatment remains a major challenge. Currently, autologous bone transplantation is still the gold standard for the treatment of large bone defects, but this treatment also faces some limitations, including limited graft supply, size issues, and donor-site morbidity [1]. Recently, biomaterials have demonstrated a potential for broad application in the treatment of large bone defect, and they have, thus, attracted great attention from researchers.

Scaffolds, osteogenic cells, and growth factors are three essential elements required for effective bone repair and regeneration. Traditional tissue-engineering methods involve loading growth factors or stem cells into a porous scaffold to enhance the bone-inducing and osteogenic abilities of the scaffold [2] [–] [4]. Bone morphogenetic protein-2 (BMP2) is a classic growth factor capable of inducing osteogenic differentiation of stem cells, with previous studies confirming a

bone-inducing role for BMP2-loaded biomaterials [5,6]. However, there are some limitations to the direct use of growth factors that can undermine their effectiveness [7] [–] [9]: 1) the need for high dosages; 2) instability during scaffold fabrication and *in vivo* application; 3) a short lifetime *in vivo*, which makes it difficult for growth factors to maintain their function for extended periods; and 4) a high cost, creating a financial burden for patients.

Conversely, cells can be functionalized to secrete growth factors by genetic engineering, thereby potentially addressing the limitations associated with their direct application [10,11]. Plasmids [12], adenoviruses [13], adeno-associated viruses [14], and lentiviruses [15] are commonly used items in this technology. Compared with other gene-transfection systems, lentiviruses allow transfer of long gene fragments with a high transfection success rate, low immunogenicity, and stable expression of the target gene for long periods [16] [–] [18]. Lentiviruses have been used in clinical trials to treat genetic and rare diseases, such as transfusion-dependent beta thalassemia and cerebral

* Corresponding author. Zhizaoju Road 639, Shanghai 200011, China.

** Corresponding author. Zhizaoju Road 639, Shanghai 200011, China.

E-mail addresses: bioshengbingy@163.com (S. Yang), ttt@sjtu.edu.cn (T. Tang).

¹ Minqi Wang and Hanjun Li contributed equally to this work.

<https://doi.org/10.1016/j.bioactmat.2020.10.022>

Received 6 August 2020; Received in revised form 22 October 2020; Accepted 25 October 2020

2452-199X/© 2020 The Authors. Production and hosting by Elsevier B.V. on behalf of KeAi Communications Co., Ltd. This is an open access article under the CC

BY-NC-ND license (<http://creativecommons.org/licenses/by-nc-nd/4.0/>).

adrenoleukodystrophy [19,20]. However, some studies have reported that application of growth factors *in vivo* might result in serious complications that introduce unpredictable risks to patients, including dysphagia, dysphonia, cervical swelling, wound complications, and ectopic bone formation [21,22]. These potential consequences require attention concerning gene expression profiles during gene therapy. The Tet-on system is a commonly used gene-control system [23,24], where gene expression is regulated by doxycycline (DOX). In the presence of DOX, the reverse tetracycline transactivator is activated along with the tetracycline response element on the promoter to initiate transcription of downstream target genes, whereas in the absence of DOX the target gene is not expressed (Scheme 1b) [25]. According to previous studies, the Tet-on system is highly sensitive to DOX, with 100% activation of target genes at very low concentrations of DOX ($1 \mu\text{g mL}^{-1}$).

Interestingly, DOX is also a broad-spectrum antibiotic that shows protective effects against infection [26]. Large bone defects frequently introduce a high risk of infection and are more difficult to treat, with increased pathogen exposure due to local open wounds and existence of an orthopedic implant, such as internal fixation device, contributing to high infection rates [27]. Additionally, colonized bacteria can impair the function of osteogenic cells, leading to delayed bone union or chronic osteomyelitis [28,29]. Therefore, it is possible that the application of DOX within a Tet-on system allows to inhibit bacterial infections and promote the repair of infectious bone defects.

Given its unique advantages in the preparation of medical implants and bone substitutes, such as high reproducibility and fabrication of customized and accurately shaped scaffolds/constructs, three-dimensional (3D)-printing technology has been widely applied [30] [–] [34]. Additionally, the development of 3D-bioprinting technology allows direct loading of living cells onto scaffolds during the fabrication process, with reports confirming cell survival and functional maintenance [35,36]. Compared with traditional tissue-engineering methods, 3D bioprinting has the following advantages: 1) long-term cultivation for cell attachment and proliferation on the scaffold is unnecessary; 2) the bioprinting method increases the amount of cells loaded in the scaffold and ensures their uniform distribution [37]; and 3) the porous structure of the printed scaffold allows sufficient nutrient transfer to the inner part of the scaffold, and also enables the embedded engineered cells to release growth factors [38]. In addition, porosity and the presence of interconnected pore networks are important for cellular migration, differentiation, and bone repair.

In this study, we fabricated a dual-functional scaffold combining genetic engineering and 3D bioprinting. A lentiviral vector harboring *BMP2* and the Tet-on system, enabling DOX-controlled expression of *BMP2*, was used to transfect cells, which were then loaded in bioink. In particular, DOX-loaded mesoporous bioactive glass (MBG) and polycaprolactone (PCL) were mixed to prepare a PCL/MBG/DOX mixture. This composite matrix and cell-loaded bioink were subsequently used for scaffolds printing. We expected that DOX released during the degradation of the bioprinted scaffold could stimulate *BMP2* expression and inhibit the growth of bacteria (Scheme 1). Furthermore, the interruption of DOX release would block the production of *BMP2*, thereby avoiding the side effects of continuous *BMP2* release.

2. Materials and methods

2.1. Materials

Puromycin and blasticidin were purchased from InvivoGen (San Diego, CA, USA). DOX and fluorescein isothiocyanate (FITC) were purchased from Sigma-Aldrich (St. Louis, MO, USA). The mouse *BMP2* ELISA kit ab119582 was purchased from Abcam (Cambridge, UK). Methacrylated gelatin (GelMA), methacrylated hyaluronic acid (HAMA), and the photoinitiator phenyl-2,4,6-trimethylbenzoylphosphonite (lithium phenyl-2,4,6-trimethylbenzoylphosphinate; LAP) were provided by StemEasy (Jiangsu, China). Calcium nitrate

tetrahydrate [$\text{Ca}(\text{NO}_3)_2 \cdot 4\text{H}_2\text{O}$], tetraethyl orthosilicate (TEOS), triethyl phosphate (TEP), and a polyethylene oxide-poly propylene oxide-polyethylene oxide triblock copolymer (PEO-PPO-PEO, P123) were all purchased from Aladdin (Shanghai, China). PCL (average molecular weight = 8.0×10^4 Da) was purchased from the Shandong Institute of Medical Instruments (Shandong, China).

2.2. Establishment of cells exhibiting controlled *BMP2* expression

To establish cells stably expressing *BMP2*, murine mesenchymal stem cells (C3H10T1/2) were seeded in six-well plates and infected with a lentiviral vector harboring Tet-on-*BMP2* and a puromycin resistance gene, as well as another lentiviral vector (mCherry) harboring a blasticidin resistance gene. Cells were grown to 50% confluence and selected with $1 \mu\text{g mL}^{-1}$ puromycin and $5 \mu\text{g mL}^{-1}$ blasticidin for 14 days. Lentiviruses were obtained from Hanbio (Shanghai, China).

2.3. Confirmation of *BMP2* expression

2.3.1. Reverse Transcription Quantitative PCR (RT-qPCR)

BMP2-transfected cells were cultured in six-well plates (1×10^5 per well) and treated with $1 \mu\text{g mL}^{-1}$ DOX for 24 h (single stimulation) or on culture days 1, 4, and 7 (multiple stimulation). For multiple stimulation, DOX was administered for 24 h, and the medium was then replaced by fresh medium without DOX. Total RNA was extracted with the Trizol reagent (Invitrogen, Carlsbad, CA, USA) on the following days for RT-qPCR analysis using the primers shown in Table 1.

2.3.2. ELISA analysis of *BMP2* levels

For both types of stimulation, supernatants were collected daily and centrifuged to remove cell debris. A *BMP2* ELISA kit was used according to the manufacturer's instructions to evaluate the levels of *BMP2* secreted by the transfected cells at different time points following DOX stimulation.

2.4. Fabrication of DOX-containing and DOX-free bioprinted scaffolds

2.4.1. Preparation of MBG powder

$\text{Ca}(\text{NO}_3)_2 \cdot 4\text{H}_2\text{O}$, TEOS, and TEP were used as the calcium, silicon, and phosphorus sources, respectively, and P123 was used as a template. The mass of each required reagent [2.8 g of $\text{Ca}(\text{NO}_3)_2 \cdot 4\text{H}_2\text{O}$, 1.46 g of TEP, 13.4 g of TEOS, and 8 g of P123] and 1 mL of HCl solution as a catalyzer were dissolved in 50 mL of absolute ethanol at room temperature and stirred with a magnetic stirrer. After incubation for 72 h to obtain a gel, the compound was dried at room temperature and then transferred to a muffle furnace and heated at $650 \text{ }^\circ\text{C}$ for 5 h after a temperature increase of $2 \text{ }^\circ\text{C min}^{-1}$. The resulting solid was ground with a mortar to obtain MBG powder. The morphology of MBG particles was assessed with transmission electron microscopy (TEM; Talos L120C, Thermo Fisher Scientific, Waltham, MA, USA). Moreover, N_2 adsorption-desorption isotherms of MBG were obtained using a TriStar 3000 porosimeter (Micromeritics, Norcross, GA, USA) under continuous adsorption at 77 K. Finally, Brunauer-Emmet-Teller and Barrett-Joyner-Halenda analyses were performed to determine the surface area, pore size, and pore volume.

2.4.2. Preparation of the PCL/MBG/DOX Mixture

DOX, MBG, and PCL (at a 2:10:88 mass ratio) were weighed, and DOX and MBG were dispersed in dH_2O . After magnetic stirring overnight, the MBG/DOX mixture in the suspension was re-lyophilized *in vacuo*. The obtained MBG/DOX powder was observed by TEM to ensure its mesoporous structure, which was expected to load DOX. The MBG/DOX powder and PCL were then transferred to a high-temperature mixer and thoroughly mixed at $90 \text{ }^\circ\text{C}$ for 30 min to obtain a uniformly mixed PCL/MBG/DOX compound, which was used for the subsequent 3D printing process.

2.4.3. Preparation of bioink containing BMP2-transfected cells

Bioink containing 5% GelMA, 1% HAMA, and 0.5% LAP was prepared according to the manufacturer's instruction. BMP2-transfected cells were digested with trypsin and collected by centrifugation at 37 °C and 300×g for 5 min, and subsequently mixed with bioink at a final concentration of 1×10^7 cells mL⁻¹. The obtained cell-loaded bioink was used for 3D bioprinting of the hybrid scaffold.

2.4.4. 3D bioprinting

The PCL/MBG/DOX and cell-loaded bioink mixtures were loaded into a tube of a Bioplotter™ 3D printer (manufacturer series, EnvisionTEC, Dearborn, MI, USA), with the following parameters: thickness of each layer, 0.32 mm; distance between each strip, 1.6 mm; printing speed, 20 mm s⁻¹ for bioink and 5 mm s⁻¹ for PCL/MBG/DOX; and pressure, 8 bar for the PCL/MBG/DOX and 2 bar for the bioink. The printing temperature for the PCL/MBG/DOX mixture and cell-loaded bioink was 90 °C and 25 °C, respectively while the diameter of the nozzle used for both materials was 0.4 mm. The PCL/MBG/DOX mixture was printed as the frame structure of the scaffold, and then the bioink was alternately printed between the stripes of PCL/MBG/DOX at each layer. Blue light at 405 nm at an intensity of 10 nm cm⁻² was used to quickly crosslink the bioink. Also, scaffolds without DOX, containing only PCL/MBG and cell-loaded bioink, were printed and used as a control.

2.5. Characterization of the bioprinted scaffold

2.5.1. DOX release kinetics

Both DOX-containing and DOX-free scaffolds were immersed in simulated body fluid at a ratio of 1 g:15 mL. At each predetermined time point (2, 6, 12, and 24 h; and 3, 5, 7, 14, and 21 days), the supernatants were collected and stored at 4 °C until further use. The absorbance of DOX standard solutions (0.01, 0.1, 1.0, 10.0, 100.0, and 500.0 µg mL⁻¹) at 250 nm was measured using a NanoDrop spectrophotometer (Thermo Fisher Scientific) to generate a standard curve, which was used to calculate the DOX concentration of the supernatant collected at different time points.

2.5.2. Scaffold surface morphology

After completing the fabrication process of the cell-loaded scaffold (day 1), we fixed the scaffold with 2.5% glutaraldehyde for 2 h and then dehydrated it with an alcohol gradient (50, 70, 80, 90, 95, and 100%; 10 min each). We then sprayed the scaffolds with gold and observed their surface morphology by scanning electron microscopy (SEM; SU8220, Hitachi, Tokyo, Japan).

2.6. Cell survival and proliferation in the scaffold

2.6.1. Confocal laser scanning microscopy

Because cells in the bioink were transfected with a vector carrying the mCherry gene, they spontaneously exhibited red fluorescence, which allowed evaluation of cell survival. After culturing the scaffolds *in vitro* for specific time periods (1 and 21 days), a confocal laser scanning microscope (CLSM; TCS SP8, Leica, Wetzlar, Germany) was used to observe the red fluorescent protein (RFP) signal from each scaffold.

2.6.2. Cell counting Kit-8 (CCK-8) assay

At 1, 7, 14 and 21 days, the medium was replaced with a 10-fold serially diluted CCK-8 reagent (Dojindo Laboratories, Tokyo, Japan). After a 2-h incubation at 37 °C, the absorbance of 100 µL of supernatant was measured at 450 nm.

2.7. Measurement of BMP2 secretion and osteogenesis by the scaffold

2.7.1. ELISA analysis of BMP2 levels

The bioprinted scaffolds were inoculated in a 12-well plate and

Table 1

Primers used in this study.

Gene		Primers (5'-3')
BMP2	F	GGGACCCGCTGTCTTCTAGT
	R	TCAAACCTCAAATTCGCTGAGGAC
β-actin	F	GGCTGTATTCCCCTCCATCG
	R	CCAGTTGGTAAACAATGCCATGT

cultured at 37 °C with 5% CO₂. The medium was changed and collected every 72 h, and then centrifuged to remove cell debris and stored at -80 °C until measurement. We used a BMP2 ELISA kit to detect BMP2 levels in the culture supernatant.

2.7.2. Alkaline phosphatase (ALP) Staining

Bone marrow-derived mesenchymal stem cells (BMSCs; 1×10^5 cells mL⁻¹) were incubated in a 12-well plate for 24 h, after which the culture medium was replaced with osteogenic induction medium [fetal bovine serum (10%), penicillin (100 IU mL⁻¹), streptomycin (100 IU mL⁻¹), dexamethasone (0.1 µM), ascorbate (50 µg mL⁻¹), and β-glycerophosphate (10 mM)]. The scaffolds were placed in the upper chamber of a Transwell plate (Corning, New York, NY, USA) and co-cultured with BMSCs. The medium was changed every 3 days, and ALP staining was performed on the 7th and 14th day.

2.7.3. Alizarin Red staining and quantitative analysis

On the 21st day of co-culture, BMSCs in the Transwell plate were fixed with 4% paraformaldehyde and stained with 500 µL of Alizarin Red staining solution for 5 min. After washing to remove excess dye, stained cells were observed under microscope. We then added a 10% cetylpyridinium chloride solution to each well to dissolve the dye, and measured the absorbance at 562 nm.

2.8. Evaluation of scaffold-specific antibacterial activity

Pathogens that commonly appear in orthopedic clinics, including methicillin-resistant *Staphylococcus aureus* (MRSA; ATCC 43300; American Type Culture Collection, Manassas, VA, USA), methicillin-resistant *Staphylococcus epidermidis* (MRSE287; isolated from the prosthetic surface of a patient with periprosthetic joint infection at the Shanghai Ninth Hospital), *Escherichia coli* (ATCC25922; American Type Culture Collection), and *Pseudomonas aeruginosa* (NCTC12903; National Collection of Type Cultures, Porton Down, UK), were used for antibacterial experiments. A single bacterial colony growing on an agar plate was transferred to 15 mL of tryptic soy broth and then shaken overnight at 37 °C and 120 rpm. The bacterial solution (1 mL) was centrifuged at 37 °C and 5000 rpm for 5 min, and bacterial concentration was adjusted to 1×10^6 CFU mL⁻¹.

2.8.1. Detection of antimicrobial kinetics

To assess the ability of the scaffolds to inhibit bacterial proliferation, scaffolds were co-cultured with the four bacterial suspensions, and absorbance at 600 nm in each well was determined at specific time points (4, 8, 18, 30, and 48 h).

2.8.2. Spread plate analysis

After cultivating the scaffold with each of the four bacterial suspensions for 24 h, the scaffolds were gently washed three times with phosphate-buffered saline (PBS) and placed in a centrifuge tube containing 2 mL of PBS for ultrasonication at 50 Hz for 10 min to dislodge adhered bacteria. The suspension in the centrifuge tubes was then serially diluted (10 fold) and plated onto agar plates for counting.

2.8.3. SEM

After 24 h, scaffolds co-cultured with bacterial suspensions underwent SEM analysis. Prior to detection, gold was sprayed on the scaffolds

following dehydration by an alcohol gradient. Bacterial distribution and morphology were observed.

2.8.4. CLSM analysis

CLSM was used to assess cellular activity according to RFP signals after co-culture with bacterial suspensions to evaluate the competitive growth of osteogenic cells and bacteria. MRSA was pretreated with FITC to evaluate variable fluorescence and avoid nonspecific adsorption of the dye on the scaffold. Briefly, we prepared a filter-sterilized buffer [FITC (0.1 mg mL^{-1}) and $\text{Na}_2\text{CO}_3/\text{NaHCO}_3\text{-NaCl}$ (0.2 M); pH 9.2] that was used to resuspend bacteria ($1 \times 10^6 \text{ CFU mL}^{-1}$), which were then incubated on ice for 30 min. Bacteria were then collected by centrifugation at 4°C and 5000 rpm and washed three times with PBS. After co-culture with the pretreated bacteria ($1 \times 10^6 \text{ CFU mL}^{-1}$) for 6 h and 24 h, the scaffolds in each well were collected and washed with PBS three times to remove nonadherent bacteria. Fluorescent signals (red and green) on the scaffold were observed by CLSM to estimate the number of living osteogenic cells and adhered bacteria, respectively.

2.9. Induction of ectopic bone formation *In vivo*

All animal experiments were examined and approved by the Animal Ethics Committee of the Shanghai Ninth People's Hospital. A heterotopic osteogenic model was established in nude mice to evaluate the osteogenic ability of the scaffolds *in vivo*. Female nude mice (6-week-old; $n = 6$ for each group) were anesthetized with an intraperitoneal injection of 1% pentobarbital sodium, and the right hind leg was fully cleaned with 2% iodine prior to surgery. A skin incision ($\sim 5 \text{ mm}$) was made, and the bioprinted scaffolds with or without DOX were placed into the subcutaneous pocket; the incision was subsequently closed with sterile suture. At 2- and 6-weeks post-surgery, X-ray (MultiFocus, Faxitron, Tucson, AZ, USA) and micro-computed tomography (micro-CT; Quantum GX, PerkinElmer, Waltham, MA, USA) images were obtained to assess the formation of bone-like tissue around the implanted scaffold. A threshold of 1415 was set to remove the image of soft tissue while clearly showing bones. Animals were sacrificed at week 6, and the scaffolds and surrounding tissues were collected for histopathologic evaluation. Briefly, the collected scaffolds and tissues were embedded in paraffin and then cut into sections ($50 \mu\text{m}$ thick). Von Kossa and Safranin O/Fast Green staining were used to detect new bone formation.

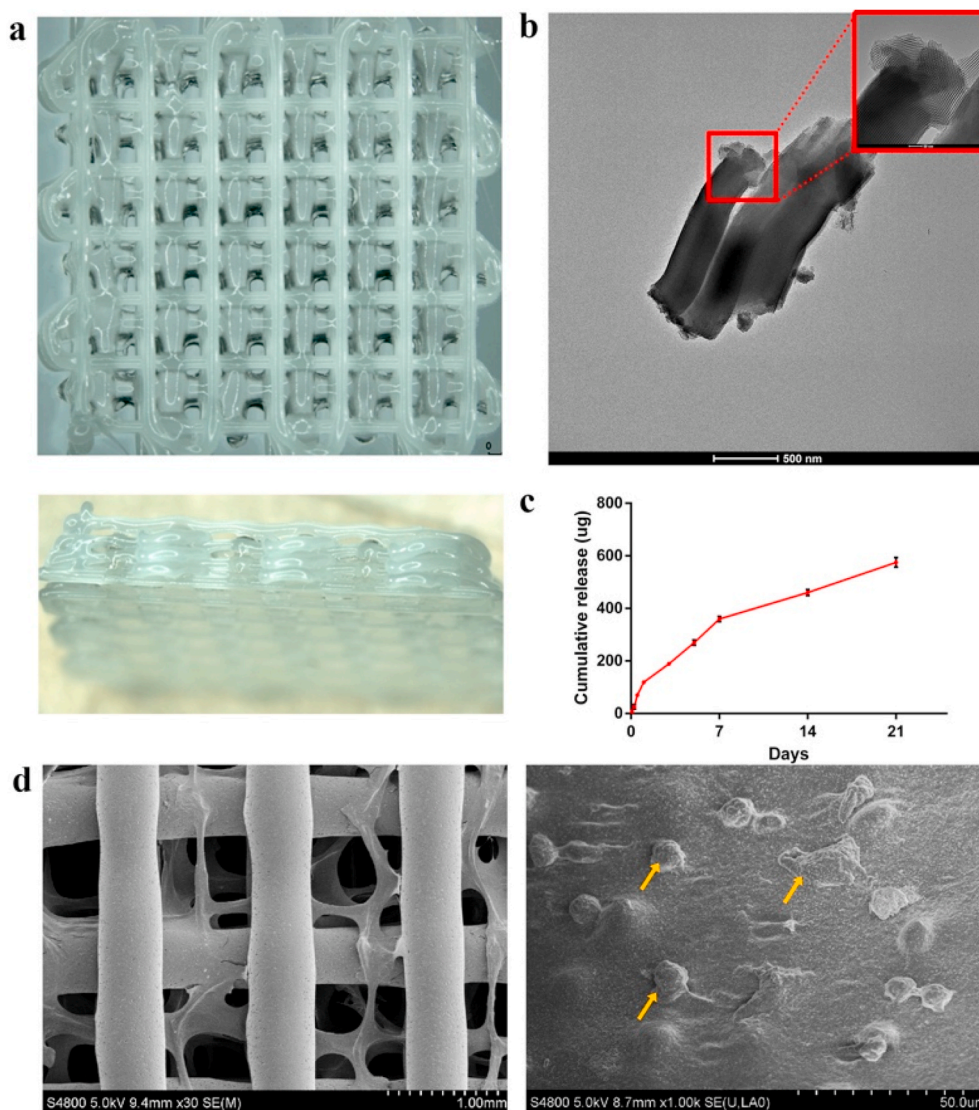


Fig. 1. Characterization of and DOX release by the bioprinted scaffold. a) Stereomicroscope image of the composite scaffold. b) TEM image of MGB powder. c) DOX-release curve within 21 days. d) SEM image of the scaffold on day1. The regular PCL/MBG/DOX and bioink cross-structures (left). Arrows (right) indicate cell spreading on the surface of the bioink.

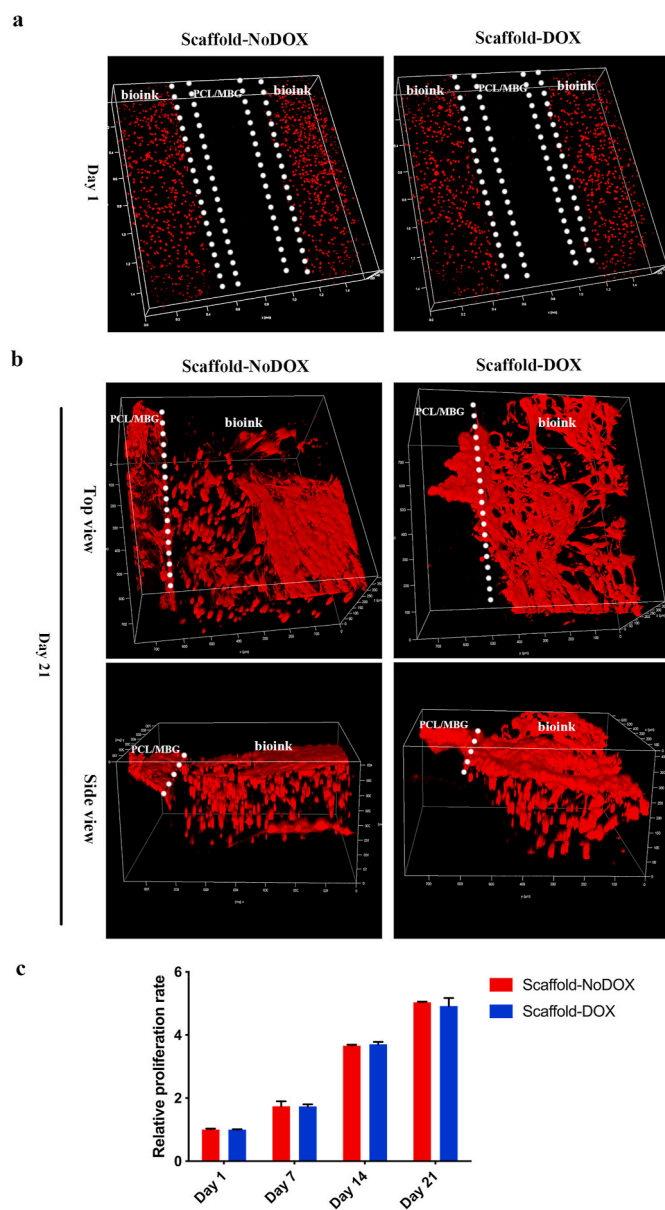


Fig. 2. Survival and proliferation of transfected C3H20T1/2 cells on the scaffold. Confocal microscopy images showing RFP-labeled cells in the scaffold on days 1 (a) and 21 (b). c) CCK-8 results showing significant cell proliferation on the scaffolds from day 1–21.

2.10. Evaluation of scaffold antibacterial activity *In vivo*

Following the same surgical and scaffold implantation procedures described in the previous subsection, we injected 100 μL of bioluminescent *S. aureus* (Xen29; ATCC12600; 1×10^6 CFU mL^{-1} ; American Type Culture Collection) at the surgical site ($n = 5$ for each group). To avoid infection-related mortality in the immunocompromised mice, we observed infection severity over a short period of time (3 days). At 1- and 3-days post-surgery, the mice were imaged with an IVIS spectrum imaging system (IVIS Lumina III, PerkinElmer), and the bioluminescent signals were quantified within a circular region of interest (ROI). Animals were sacrificed on day 3, and the scaffolds were collected for evaluation. Briefly, the scaffolds were ultrasonicated at 50 Hz for 10 min, the supernatants were serially diluted (10 fold), and bacteria was counted using the spread plate method.

2.11. Statistical analysis

Data are expressed as mean \pm standard deviation. *In vitro* experiments were performed in triplicate. The *t*-test and ANOVA analyses were used to compare values among groups. Statistical analyses were performed using SPSS (v.19.0; IBM Corp., Armonk, NY, USA), and results displaying $p < 0.05$ were considered statistically significant.

3. Results

3.1. BMP2 controlled release from transfected cells

Most cells showed a strong RFP signal, demonstrating successful transfection of the mCherry lentivirus (Fig. S1a). Our preliminary results demonstrated that DOX significantly stimulated BMP2 expression at a dose of 1000 ng mL^{-1} . Moreover, the results of PCR and ELISA confirmed DOX-controlled BMP2 expression and BMP2 release from transfected cells. After DOX stimulation, BMP2 expression levels increased rapidly within 1 day, reaching up to ~ 30 -fold higher levels than those in control scaffolds, and then rapidly decreased after removal of DOX (Fig. S1b). Additionally, this trend was observed following repeated DOX stimulation (Fig. S1c). Furthermore, ELISA results indicated that BMP2 production increased significantly from the second day after DOX stimulation, reaching a peak level on day 7 (Fig. S1d).

3.2. Morphological characteristics of bioprinted scaffolds and their drug release

The stereomicroscope image in Fig. 1a shows that the scaffold was composed by strips of PCL/MBG/DOX and bioink, which showed a regular structure with uniform pores. Also, the prepared MBG/DOX powder was observed by TEM, and clearly showed an inner mesoporous structure (Fig. 1b). Further, the porosity of MBG powder was investigated using nitrogen sorption analyses. The pore size, surface area, and pore volume of MBG were found to be approximately 6.66 nm, 328.58 $\text{m}^2 \text{g}^{-1}$, and 0.578 $\text{cm}^3 \text{g}^{-1}$, respectively (Fig. S2). In addition, the PCL/MBG/DOX scaffold demonstrated good mechanical properties, with a compressive modulus of 82.455 ± 18.887 MPa (Fig. S3). Evaluation of DOX level according to its absorption peak at 250 nm revealed a burst release of $\sim 150 \mu\text{g}$ within 1 day, followed by a slow release to reach $\sim 400 \mu\text{g}$ at day 7. In the subsequent 2 weeks, the cumulative released DOX in this period was $\sim 200 \mu\text{g}$ (Fig. 1c).

SEM images of the scaffold surface morphology on day 1 are shown in Fig. 1d. In addition to the regular strips, shrunken strips were observed, representing dehydrated cell-loaded bioink. Additionally, high magnification revealed the presence of numerous sphere-like cells on the bioink sheet.

3.3. Cell survival and proliferation on the scaffold

Fig. 2a shows a CLSM image of one bioprinted scaffold on day 1 after fabrication. Red fluorescence, spontaneously emitted by active cells, was uniformly distributed within the bioink, confirming successful loading of living cells inside the scaffold; however, no cells were found in the frame strips. Fig. 2b shows a 3D-reconstructed fluorescent image of the scaffold after 21 days of *in vitro* culture. Strong red fluorescent signals and dense cell sheets were found across the whole scaffold surface, suggesting sustained cell survival, cells migration, and interconnection. The results of CCK-8 assays confirmed cell proliferation in the scaffold (Fig. 2c), at a ~ 5 -fold higher rate on day 21 relative to that on the day of printing.

3.4. *In vitro* antibacterial activity of the scaffolds

In addition to stimulating BMP2 expression, sustained release of DOX from the bioprinted scaffold exerted broad-spectrum antibiotic activity.

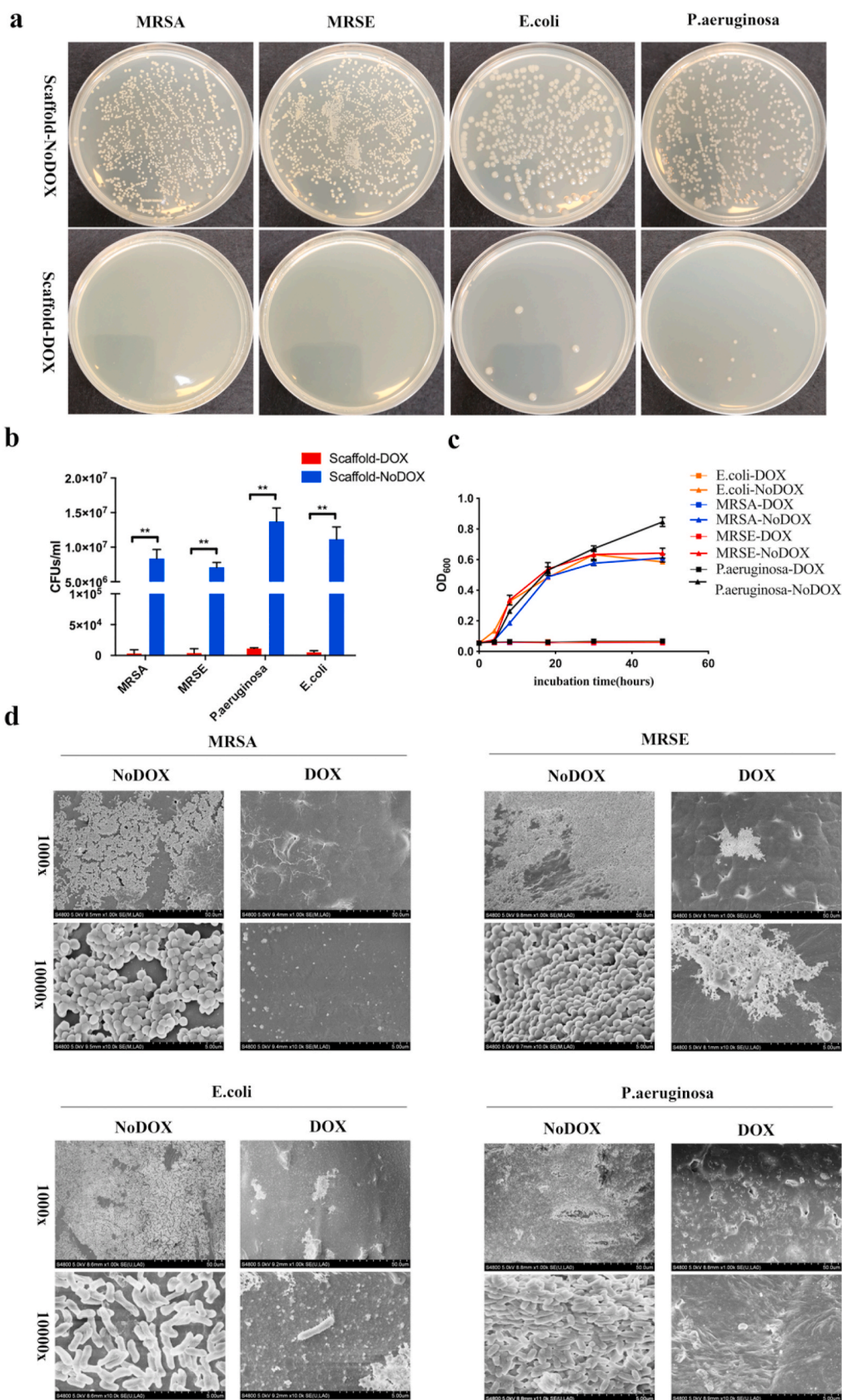


Fig. 3. Antibacterial efficiency of the biprinted scaffold. a,b) Spread plate results showing that the DOX-containing scaffold significantly inhibited bacterial adhesion and proliferation on its surface. c) Results of absorbance of surrounding medium showing broad-spectrum bactericidal effect of scaffolds with DOX. d) SEM images showing that DOX significantly inhibited bacterial adhesion to the scaffold surface. **p < 0.01.

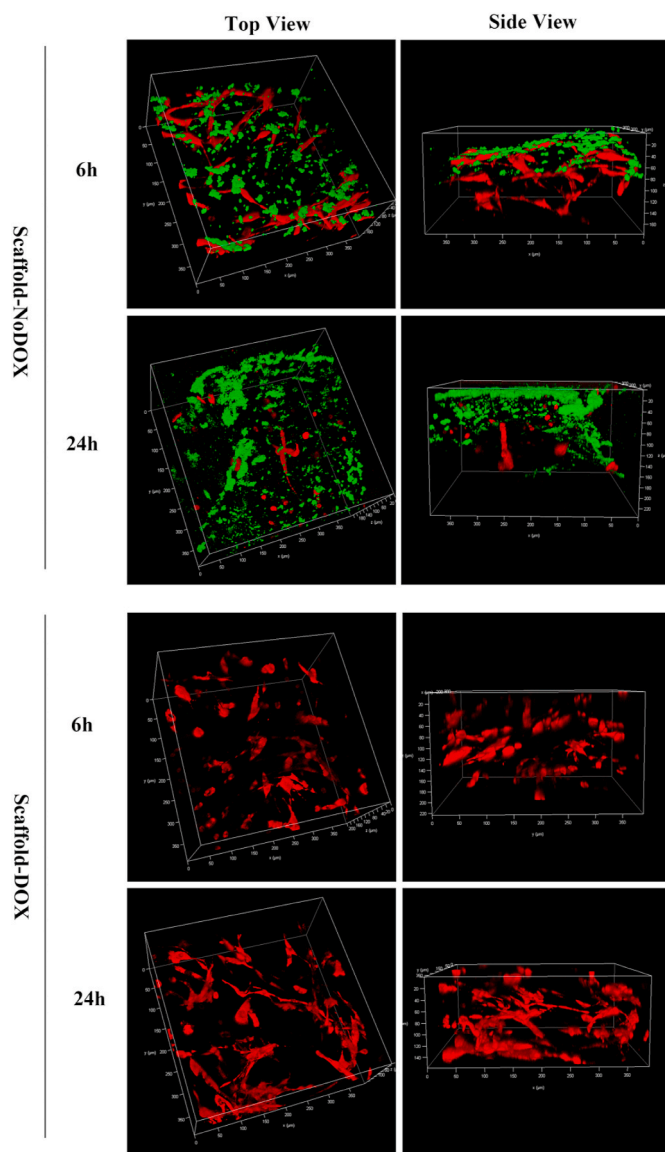


Fig. 4. CLSM images of scaffolds. Co-localization of osteogenic cells and bacteria on the scaffold by CLSM revealed bacterial adherence to the surface of DOX-free scaffolds and growth into the hydrogel. DOX-containing scaffolds prevented bacterial adhesion and ensured osteogenic cell survival in the scaffold. Red signals indicate RFP-labeled C3H20T1/2 cells, and green signals indicated FITC-pretreated MRSA. (For interpretation of the references to color in this figure legend, the reader is referred to the Web version of this article.)

Indeed, after co-culturing of scaffolds with bacterial suspensions, absorbance monitoring showed stronger inhibition of four types of bacteria upon using the scaffold containing DOX than the control scaffold (Fig. 3c). In addition, spread plate analysis showed a decrease in the number of bacteria adhering to the scaffold surface (Fig. 3a and b). These results indicated that these scaffolds exhibited broad-spectrum bactericidal activity against both gram-positive and gram-negative bacteria. Additionally, SEM analysis (Fig. 3d) confirmed that few bacteria adhered to the surface of the DOX-containing scaffold. In contrast, the surface of the scaffold without DOX was almost completely occupied by each of the four bacterial strains.

Interestingly, CLSM images showed competitive growth between osteogenic cells and existing bacteria (Fig. 4, Fig. S4). In fact, we observed green fluorescence on the surface of the control scaffold without DOX, with most bacteria localized on the shallow surface of the bioink at 6 h, while carrying out deeper invasion at 24 h accompanied by

dense biofilm formation. Additionally, RFP-labeled osteogenic cells co-localized with green bacteria inside the scaffold without DOX at 6 h; however, the number of osteogenic cells diminished over time until very few of them were observed at 24 h, indicating that the invading bacteria had killed the osteogenic cells and thus impaired the osteogenic potential of the bioprinted scaffold. By contrast, despite co-culture with bacteria, DOX-containing scaffolds showed no bacteria on the surface but great survival of osteogenic cells inside the scaffold at 6 h, followed by their subsequent spreading and connection at 24 h. These findings showed that DOX-containing scaffolds inhibited bacterial growth, thereby promoting the survival and proliferation of osteogenic cells in the scaffold.

3.5. *In vitro* osteogenesis by the bioprinted scaffolds

After release of DOX by the scaffolds, *BMP2* expression in cells embedded in the bioink was followed by *BMP2* release. Indeed, ELISA showed an increasing *BMP2* level after DOX release, reaching a maximum value on day 12 and maintaining a high level until day 21 (Fig. 5d). We evaluated the osteogenic activity of scaffolds by ALP and Alizarin Red staining (Fig. 5a and b). After 7 days of co-cultivation with scaffolds not containing DOX, BMSCs exhibited stronger ALP staining than those co-cultured with osteogenic supplements (OM group) only, suggesting that even without DOX, other components in the scaffold promoted osteogenic differentiation to some extent. Additionally, at days 7 and 14 after co-culture with scaffolds containing DOX, BMSCs showed much more intense ALP staining compared to both OM and DOX-free scaffold groups. Moreover, Alizarin Red staining of BMSCs in scaffolds containing DOX was more prominent than in the other two groups, and its quantification indicated that such difference was significant ($p < 0.01$) (Fig. 5c).

3.6. *In vivo* ectopic osteogenesis by the bioprinted scaffold

We used X-ray images to assess ectopic bone formation around the scaffold in the right hind subcutaneous region of nude mice after implanting (Fig. S5). Observation at 1-day and 2- and 6-weeks post-surgery revealed that animals implanted with scaffolds containing DOX showed small amounts of high-density shadows at 2 weeks, although their distribution was dispersive and irregular. At 6-weeks post-surgery, local high-density shadows expanded and resembled square-like structures consistent with the shape of implanted scaffolds. This suggested that ectopic osteogenesis had occurred around the DOX-containing scaffold. However, in animals implanted with scaffolds without DOX, we observed no high-density shadows at 1-day and 2-weeks post-surgery and only minimal amounts of small, scattered high-density shadows at 6 weeks.

In vivo micro-CT further confirmed the ectopic osteogenic efficiency of the bioprinted scaffolds (Fig. 6a and b). The green pseudo-color indicates an increased local density of ectopic osteogenesis at the early stage in animals implanted with DOX-containing scaffolds. At 6-weeks post-surgery, we observed increased green signals at the right hind operated region, with shapes similar to those of the implanted scaffolds. By contrast, animals implanted with DOX-free scaffolds showed only a small amount of green pseudo-color signals, even after 6 weeks. These results confirmed significant ectopic osteogenesis at 2- and 6-weeks post-surgery in animals implanted with DOX-containing scaffolds.

We then performed histopathologic analysis of the subcutaneous scaffolds and surrounding tissues at 6-weeks post-surgery (Fig. 6c). In tissues from animals implanted with DOX-containing scaffolds, we observed areas strongly stained with Von Kossa staining in tissue surrounding the bioprinted scaffold (red box), accompanied by areas stained with Safranin O/Fast Green, suggesting the presence of newly formed bone. Additionally, we observed areas stained with both Von Kossa and Safranin O/Fast Green staining inside the bioink (blue box), indicating possible osteo-chondrogenic differentiation. By contrast,

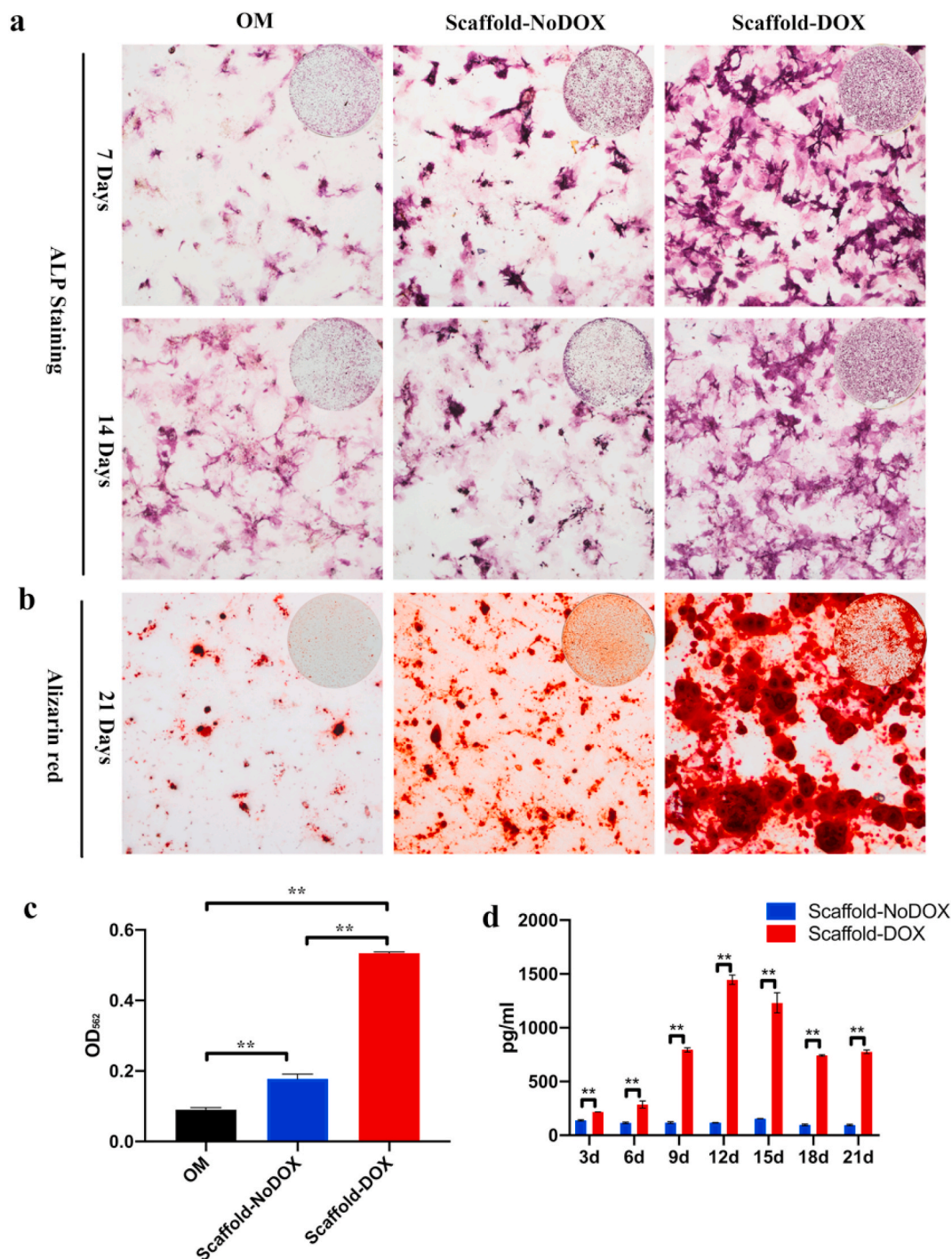


Fig. 5. Effect of the biprinted scaffolds on osteogenic differentiation of BMSCs. a) ALP staining after 7 and 14 days of culture. The OM group contained only osteogenic supplements. b) Alizarin Red staining after 21 days of co-culture. c) Quantitative analysis of Alizarin Red staining. d) BMP2 secretion from scaffolds according to ELISA. ** $p < 0.01$. (For interpretation of the references to color in this figure legend, the reader is referred to the Web version of this article.)

minimal Von Kossa and Safranin O/Fast Green staining were observed in either the tissues surrounding the DOX-free scaffold or the bioink inside the scaffold.

3.7. *In vivo* antibacterial properties of the biprinted scaffold

We constantly monitored the antibacterial activity of these biprinted scaffolds at local infectious sites *in vivo* by observing the fluorescence emission from bioluminescent *S. aureus* (Xen29). On the day of surgery, we observed clear signals in both animals implanted with DOX-

containing or DOX-free scaffolds, confirming successful injection of bacteria at the surgical site. At 3-days post-surgery, bacteria emitted sustained strong fluorescent signals at the surgical site of animals implanted with DOX-free scaffolds, indicating the existence of infection, whereas no bacterial fluorescent signal was observed in animals implanted with DOX-containing scaffolds (Fig. 7a). Quantitative analysis of fluorescence in the ROI within local infection sites indicated no significant difference between groups at 1-day post-surgery; however, on day 3, signal intensity around DOX-containing scaffolds was significantly lower than around DOX-free scaffolds ($p < 0.05$) (Fig. 7b). After

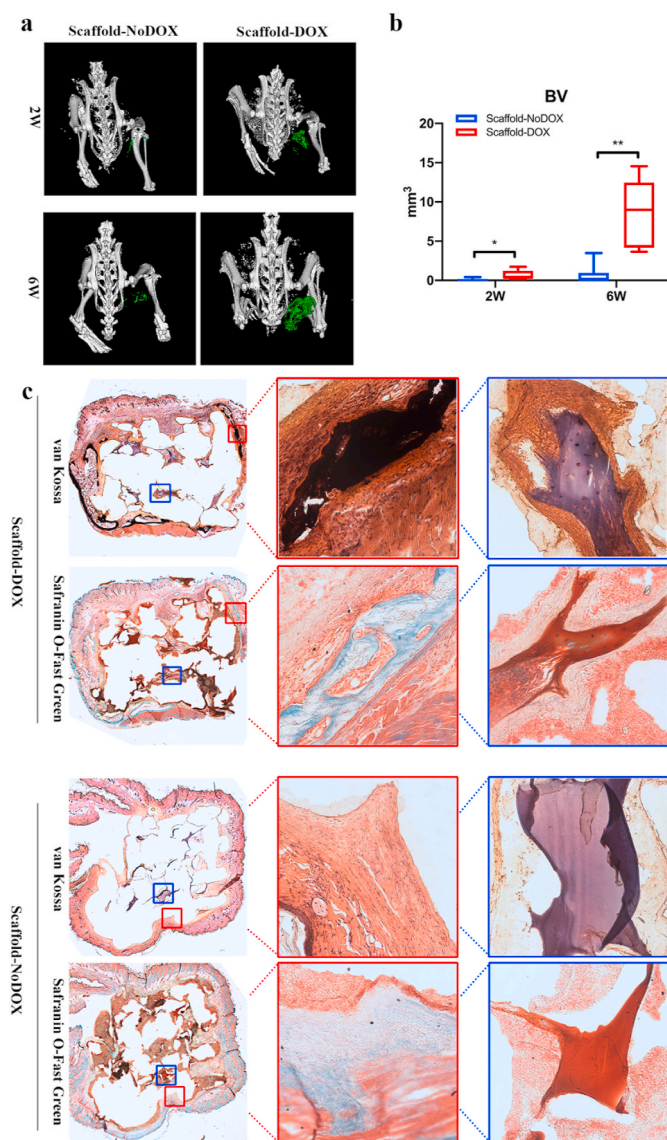


Fig. 6. Micro-CT images and histologic analysis of ectopic osteogenesis in nude mice. a) Reconstructed *in vivo* micro-CT image. Green areas indicate local high-density tissue in the scaffold representing newly formed bone. b) Statistical analysis indicated significantly higher amounts of bone formed by DOX-containing scaffolds relative to that by DOX-free scaffolds. c) Von Kossa and Safranin O/Fast Green staining were used to evaluate ectopic osteogenesis. Areas of deep Von Kossa staining (black) and Safranin O/Fast Green staining represent newly formed bone-like tissue. Red boxes indicate tissue around the bioprinted scaffolds, and blue boxes indicate areas of bioink inside the scaffold. * $p < 0.05$, ** $p < 0.01$. (For interpretation of the references to color in this figure legend, the reader is referred to the Web version of this article.)

sacrificing the animals, bacteria grown on the subcutaneous scaffolds were counted, revealing almost no bacteria in DOX-containing scaffolds and a large number of bacteria in control scaffolds (Fig. 7c).

4. Discussion

In this study, we fabricated a 3D-bioprinted scaffold containing living cells capable of controlled expression and release of BMP2 to promote bone formation. Given the possible complications caused by long-term application of BMP2, the expression system involved DOX-mediated stimulation of *BMP2* expression. Because DOX is a broad-spectrum antibiotic, the 3D-bioprinted scaffold also exhibited antibacterial activity, which protected the osteogenic cells from bacterial

infection.

First, we assessed the mechanical properties of the 3D-printed PCL/MBG/DOX scaffold containing cell-loaded bioink and found that it showed a compressive modulus of 82.455 ± 18.887 MPa (Fig. S3), which falls within the suggested compressive modulus range for optimal bone tissue regeneration (10–1500 MPa) [39]. Scaffolds with good mechanical properties are helpful in the process of large bone defect healing, as they can ensure stability in the site of bone defect, and hence, they help the ingrowth of new bone.

SEM images showed that there were some cells on the surface of the bioink, confirming successful loading of engineered cells into the scaffold using 3D bioprinting (Fig. 1d). Moreover, CLSM images on day 1 confirmed the presence of a large number of cells uniformly distributed in the bioink and expressing a strong RFP signal, indicating good cellular viability. These early-stage images also showed that cells assumed a sphere-like shape, demonstrating that cells were encased in bioink and not already spread across the scaffold. Furthermore, CLSM images showed that after prolonged culture of scaffolds cells, the cells spread widely, especially those located near the surface of bioink. In addition, these cells proliferated remarkably and migrated across the scaffold. This observation was also confirmed using CCK-8 assays showing that after 21 days of culture the number of cells in the scaffold increased by almost 5-fold relative to day 1. These findings were consistent with a previous study discussing the importance of the porous structure of 3D-printed scaffolds for cell survival and proliferation [38,40]. In fact, the bioprinted scaffold fabricated in our study had widely distributed pores of uniform size, which allowed nutrient exchange and growth factor secretion. Additionally, the cells were protected by the bioink, which demonstrated good structural stability and retained the cells within the scaffold for an extended period of time, and also protected the cells from damage during the process of material preparation and cultivation *in vitro* and *in vivo* [41].

Ensuring cell survival was the primary function of the scaffold, whereas successful synthesis and secretion of BMP2 by cells was key to its osteo-inductive ability. In our previous study, we demonstrated that the bioink used in this study can maintain the viability and function of loaded cells for a long period of time [42]. The benefits of using this bioink were demonstrated again in this study. In fact, the cells embedded in the scaffold not only survived or proliferated considerably within 21 days, but also maintained their functions, secreting BMP2 continuously and markedly, which promoted the osteogenic differentiation of co-cultured BMSCs. Moreover, our results showed that cells were successfully transfected by the lentiviral Tet-on vector and exhibited controlled expression of *BMP2* under DOX stimulation, followed by the secretion of BMP2 into the supernatant during *in vitro* cultivation. In particular, we observed significant increases in the levels of BMP2 secreted by the bioprinted scaffold on day 3, with these levels increasing further on day 9. We confirmed that BMP2 secretion occurred only under DOX stimulation, which may allow to avoid the complications related to BMP2 overuse [7,21]. DOX was firstly loaded into the mesopore structure of MBG and then fully mixed with molten PCL to create MBG/DOX microspheres encased by PCL. This allowed the scaffold to sustainably release DOX within 21 days, which promoted continuous secretion of BMP2 to induce and accelerate bone repair.

DOX exhibits antibacterial activity [43], and we confirmed that DOX could inhibit the growth of several pathogenic bacteria common in orthopedic settings, including gram-positive and -negative bacteria. Bone defects related to severe trauma are often accompanied by open wounds, which increase the risk of bacterial contamination and infection [44,45]. Moreover, scaffolds can provide a surface for bacterial adhesion, thereby allowing bacteria to aggregate and proliferate on the surface of the scaffold, forming biofilm and invading osteoblasts subsequently [27,28]. In this study, we showed that DOX-containing scaffolds significantly inhibited bacterial adhesion and proliferation while promoting the survival and proliferation of osteogenic cells in the scaffold, and thus help cells compete against bacteria [46]. These findings support the use

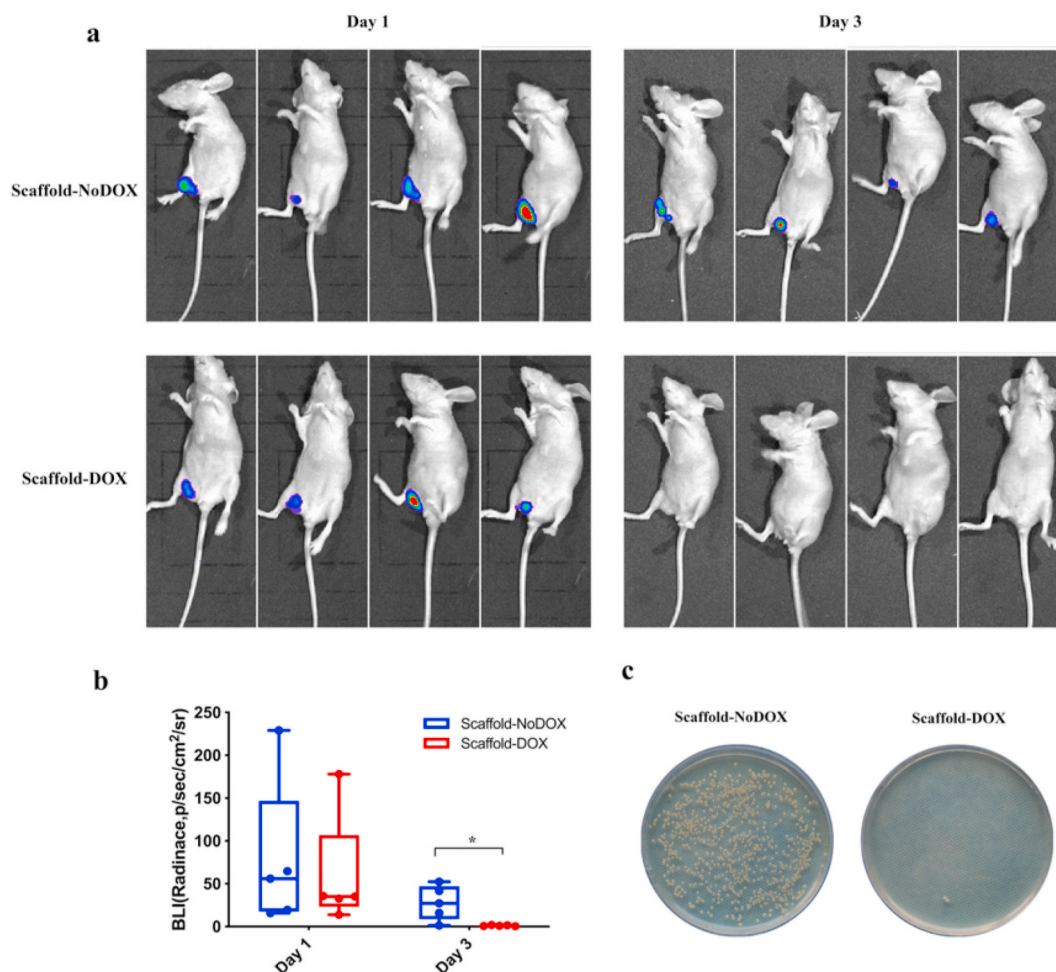


Fig. 7. The antibacterial activity of the bioprinted scaffolds in nude mice. a) *In vivo* imaging of bioluminescent signals of bacteria at days 1 and 3 after implantation, respectively. b) Quantitative analysis and comparison of bioluminescence intensity. c) Culture of bacteria released from each scaffold. * $p < 0.05$.

of this bioprinted scaffold to reduce the infection rate and promote the repair of bone defects in bacteria-contaminated environments. Furthermore, our group had previously demonstrated the antibacterial properties of a novel material named quaternised chitosan, which showed great antimicrobial efficacy and good biocompatibility. We have successfully produced several quaternised chitosan-based materials for potential clinical use [47] [–] [49]. Comparing with quaternised chitosan, DOX has a broader antibacterial spectrum and is currently used widely in clinical practice. Therefore, considering its possible combination with the Tet-on system and its wide antibacterial spectrum, DOX was deemed easier for clinical translation, and thus chosen as the antibacterial compound in this study.

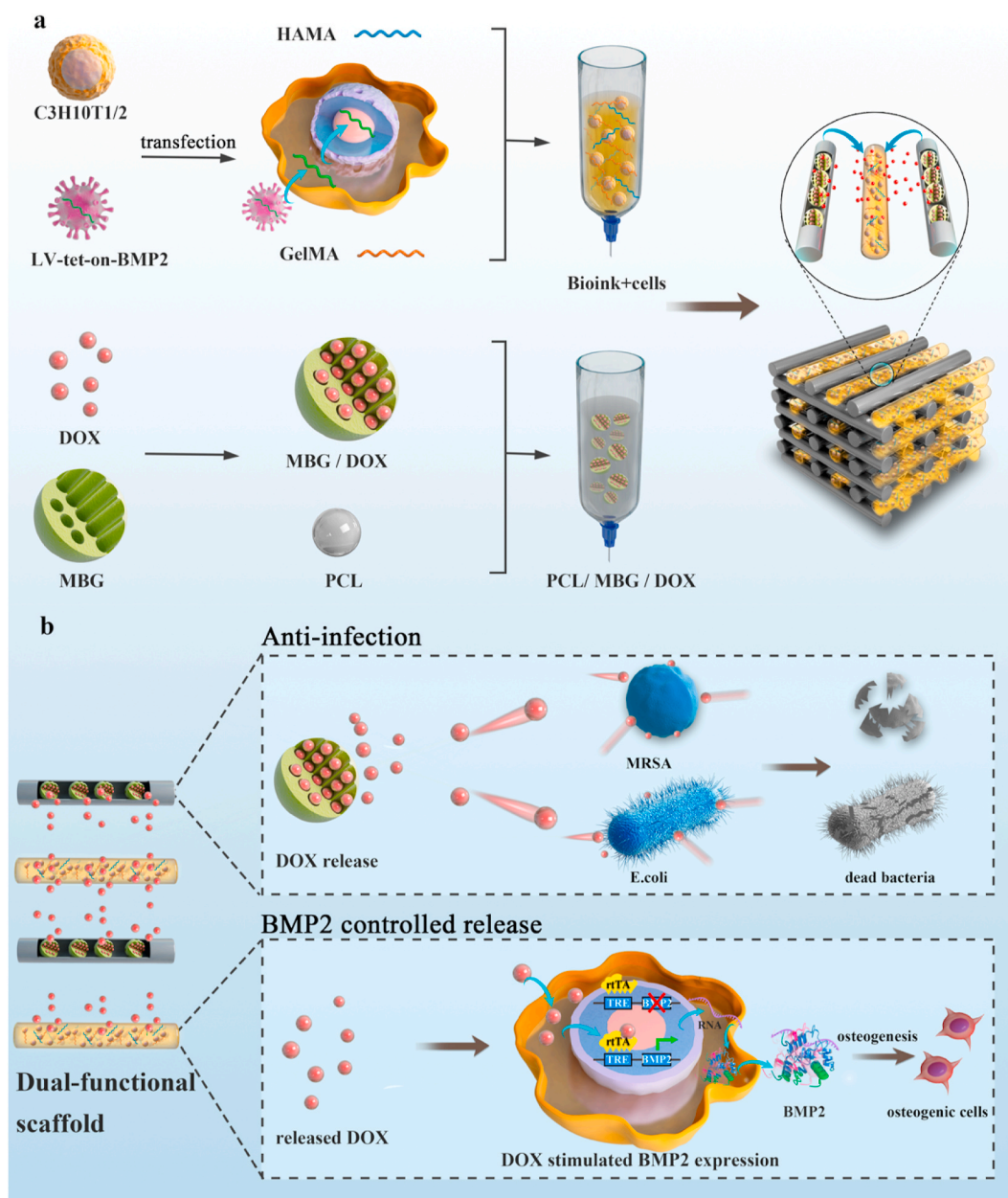
In vitro co-culture with BMSCs showed that the scaffolds significantly promoted osteogenic differentiation and bone regeneration. Considering that after scaffold implantation graft rejection may occur, due to the presence of the non-autogenous mesenchymal stem cell line C3H10T1/2 in the bioprinted scaffold, possibly leading to cell death [50], we chose to assess the *in vivo* osteogenic potential of DOX-containing scaffolds in an ectopic osteogenesis model in nude mice, which have been deemed suitable for the implantation of biomaterial loaded with C3H10T1/2 cells [51]. In future studies, we will use autologous BMSCs to build engineered cells, construct biological 3D-printed scaffolds containing transfected autologous stem cells, and explore their application potential in large bone defect repair, in order to establish the use of these excellent bone-healing scaffolds in clinical applications.

5. Conclusion

The results of this study demonstrated the efficacy of a DOX-containing scaffold derived from the combination of genetic engineering and 3D bioprinting in bone repair and prevention of infections, through its osteo-inductive ability and antibacterial potential. Therefore, these scaffolds are clinically applicable for repairing infectious bone defects. The method described in this study allowed controlled release of the growth factor BMP2 from the scaffold according to the presence of DOX, thereby inducing osteogenic differentiation and new bone formation while inhibiting bacterial infection.

CRedit authorship contribution statement

Minqi Wang: Conceptualization, Data curation, Formal analysis, Validation, Writing - original draft, Writing - review & editing. **Hanjun Li:** Formal analysis, Validation, Methodology, Supervision, Writing - review & editing. **Yiqi Yang:** Investigation, Validation, Methodology. **Kai Yuan:** Investigation, Methodology. **Feng Zhou:** Methodology, Validation, Formal analysis. **Haibei Liu:** Methodology, Formal analysis, Resources. **Qinghui Zhou:** Methodology, Resources. **Shengbing Yang:** Conceptualization, Formal analysis, Methodology, Resources, Writing - review & editing. **Tingting Tang:** Conceptualization, Funding acquisition, Project administration, Supervision, Writing - review & editing.



Scheme 1. The 3D-bioprinted scaffold with cells exhibiting DOX-controlled *BMP2* expression. a) Construction of the transfected cells that can express *BMP2* based on the Tet-on expression control system, and fabrication of 3D bioprinting scaffold that contains composite of PCL/MBG/DOX and engineering cells within the bioink. b) Mechanisms of antibacterial properties and *BMP2* controlled release ability of the bioprinting dual-functional scaffold.

Declaration of competing interest

The authors declare that they have no competing financial interests or personal relationships that could have appeared to influence the work reported in this paper.

Acknowledgements

This study was supported by the National Key R&D Program (grant no. 2016YFC1102100), a NSFC grant (grant no.81921002), and the Shanghai Science and Technology Development Fund (grant no. 18DZ2291200 and 18441902700).

Appendix A. Supplementary data

Supplementary data to this article can be found online at <https://doi.org/10.1016/j.bioactmat.2020.10.022>.

[org/10.1016/j.bioactmat.2020.10.022](https://doi.org/10.1016/j.bioactmat.2020.10.022).

References

- [1] J. Wang, D. Wu, Z. Zhang, J. Li, Y. Shen, Z. Wang, Y. Li, Z.Y. Zhang, J. Sun, Biomimetically ornamented rapid prototyping fabrication of an apatite-collagen-polycaprolactone composite construct with nano-micro-macro hierarchical structure for large bone defect treatment, *ACS Appl. Mater. Interfaces* 7 (47) (2015) 26244–26256.
- [2] J.E. Song, J. Tian, Y.J. Kook, M. Thangavelu, J.H. Choi, G. Khang, A BMSCs-laden quercetin/duck's feet collagen/hydroxyapatite sponge for enhanced bone regeneration, *J. Biomed. Mater. Res.* 108 (3) (2020) 784–794.
- [3] L.M. Caballero Aguilar, S.M. Silva, S.E. Moulton, Growth factor delivery: defining the next generation platforms for tissue engineering, *J. Contr. Release* 306 (2019) 40–58.
- [4] W. Lin, L. Xu, S. Lin, L. Shi, B. Wang, Q. Pan, W.Y.W. Lee, G. Li, Characterisation of multipotent stem cells from human peripheral blood using an improved protocol, *J. Orthop. Translat.* 19 (2019) 18–28.

- [5] F.B. Basmanav, G.T. Kose, V. Hasirci, Sequential growth factor delivery from complexed microspheres for bone tissue engineering, *Biomaterials* 29 (31) (2008) 4195–4204.
- [6] D.M. Gibbs, C.R. Black, G. Hulsart-Billstrom, P. Shi, E. Scarpa, R.O. Oreffo, J. I. Dawson, Bone induction at physiological doses of BMP through localization by clay nanoparticle gels, *Biomaterials* 99 (2016) 16–23.
- [7] A.W. James, G. LaChaud, J. Shen, G. Asatrian, V. Nguyen, X. Zhang, K. Ting, C. Soo, A review of the clinical side effects of bone morphogenetic protein-2, *Tissue Eng. B Rev.* 22 (4) (2016) 284–297.
- [8] K.W. Lo, T. Jiang, K.A. Gagnon, C. Nelson, C.T. Laurencin, Small-molecule based musculoskeletal regenerative engineering, *Trends Biotechnol.* 32 (2) (2014) 74–81.
- [9] Q. Zhang, J.H. Oh, C.H. Park, J.H. Baek, H.M. Ryoo, K.M. Woo, Effects of dimethylolallylglycine-embedded poly(ϵ -caprolactone) fiber meshes on wound healing in diabetic rats, *ACS Appl. Mater. Interfaces* 9 (9) (2017) 7950–7963.
- [10] T.T. Tang, X.L. Xu, K.R. Dai, C.F. Yu, B. Yue, J.R. Lou, Ectopic bone formation of human bone morphogenetic protein-2 gene transfected goat bone marrow-derived mesenchymal stem cells in nude mice, *Chin. J. Traumatol.* 8 (1) (2005) 3–7.
- [11] B. Yue, B. Lu, K.R. Dai, X.L. Zhang, C.F. Yu, J.R. Lou, T.T. Tang, BMP2 gene therapy on the repair of bone defects of aged rats, *Calcif. Tissue Int.* 77 (6) (2005) 395–403.
- [12] S. Wang, C. Yan, X. Zhang, D. Shi, L. Chi, G. Luo, J. Deng, Antimicrobial peptide modification enhances the gene delivery and bactericidal efficiency of gold nanoparticles for accelerating diabetic wound healing, *Biomater. Sci.* 6 (10) (2018) 2757–2772.
- [13] X. Liu, C. Bao, H.H.K. Xu, J. Pan, J. Hu, P. Wang, E. Luo, Osteoprotegerin gene-modified BMSCs with hydroxyapatite scaffold for treating critical-sized mandibular defects in ovariectomized osteoporotic rats, *Acta Biomater.* 42 (2016) 378–388.
- [14] F. Collaud, G. Bortolussi, L. Guianvarc'h, S.J. Aronson, T. Bordet, P. Veron, S. Charles, P. Vidal, M.S. Sola, S. Rundwasser, D.G. Dufour, F. Lacoste, C. Luc, L. V. Wittenberghe, S. Martin, C. Le Bec, P.J. Bosma, A.F. Muro, G. Ronzitti, M. Hebben, F. Mingozzi, Preclinical development of an AAV8-hUGT1A1 vector for the treatment of crigler-najjar syndrome, *Mol. Ther. Methods Clin. Dev.* 12 (2019) 157–174.
- [15] P. Shrimali, M. Peter, A. Singh, N. Dalal, S. Dakave, S.V. Chiplunkar, P. Tayalia, Efficient in situ gene delivery via PEG diacyrilate matrices, *Biomater. Sci.* 6 (12) (2018) 3241–3250.
- [16] N. Tandon, K.N. Thakkar, E.L. LaGory, Y. Liu, A.J. Giaccia, Generation of stable expression mammalian cell lines using lentivirus, *Bio. Protoc.* 8 (21) (2018).
- [17] Y. Dang, R. Loewen, H.A. Parikh, P. Roy, N.A. Loewen, Gene transfer to the outflow tract, *Exp. Eye Res.* 158 (2017) 73–84.
- [18] Y.H. Chen, M.S. Keiser, B.L. Davidson, Viral vectors for gene transfer, *Curr. Protoc. Mouse Biol.* 8 (4) (2018) e58.
- [19] S. Knight, M. Collins, Y. Takeuchi, Insertional mutagenesis by retroviral vectors: current concepts and methods of analysis, *Curr. Gene Ther.* 13 (3) (2013) 211–227.
- [20] M.A. Goodman, P. Malik, The potential of gene therapy approaches for the treatment of hemoglobinopathies: achievements and challenges, *Ther. Adv. Hematol.* 7 (5) (2016) 302–315.
- [21] C.A. Tannoury, H.S. An, Complications with the use of bone morphogenetic protein 2 (BMP-2) in spine surgery, *Spine J.* 14 (3) (2014) 552–559.
- [22] Y.D. Wen, W.M. Jiang, H.L. Yang, J.H. Shi, Exploratory meta-analysis on dose-related efficacy and complications of rhBMP-2 in anterior cervical discectomy and fusion: 1,539,021 cases from 2003 to 2017 studies, *J. Orthop. Translat.* 24 (2020) 166–174.
- [23] A.T. Das, L. Tenenbaum, B. Berkhout, Tet-on systems for doxycycline-inducible gene expression, *Curr. Gene Ther.* 16 (3) (2016) 156–167.
- [24] L. Cui, J. Zhang, J. Zou, X. Yang, H. Guo, H. Tian, P. Zhang, Y. Wang, N. Zhang, X. Zhuang, Z. Li, J. Ding, X. Chen, Electroactive composite scaffold with locally expressed osteoinductive factor for synergistic bone repair upon electrical stimulation, *Biomaterials* 230 (2020) 119617.
- [25] Y. Zhang, Y. Chen, Y. Fu, C. Ying, Y. Feng, Q. Huang, C. Wang, D.S. Pei, D. Wang, Monitoring tetracycline through a solid-state nanopore sensor, *Sci. Rep.* 6 (2016) 27959.
- [26] A.K. Thabit, D.F. Fatani, M.S. Bamakhrama, O.A. Barnawi, L.O. Basudan, S. F. Alhejailli, Antibiotic penetration into bone and joints: an updated review, *Int. J. Infect. Dis.* 81 (2019) 128–136.
- [27] C.R. Ariola, D. Campoccia, L. Montanaro, Implant infections: adhesion, biofilm formation and immune evasion, *Nat. Rev. Microbiol.* 16 (7) (2018) 397–409.
- [28] J. Josse, F. Velard, S.C. Gangloff, *Staphylococcus aureus* vs. osteoblast: relationship and consequences in osteomyelitis, *Front Cell Infect. Microbiol.* 5 (2015) 85.
- [29] J. Josse, F. Valour, Y. Maali, A. Diot, C. Batailler, T. Ferry, F. Laurent, Interaction between *Staphylococcal* biofilm and bone: how does the presence of biofilm promote prosthesis loosening? *Front. Microbiol.* 10 (2019) 1602.
- [30] Y. Yang, L. Chu, S. Yang, H. Zhang, L. Qin, O. Guillaume, D. Eglin, R.G. Richards, T. Tang, Dual-functional 3D-printed composite scaffold for inhibiting bacterial infection and promoting bone regeneration in infected bone defect models, *Acta Biomater.* 79 (2018) 265–275.
- [31] L. Zhang, G. Yang, B.N. Johnson, X. Jia, Three-dimensional (3D) printed scaffold and material selection for bone repair, *Acta Biomater.* 84 (2019) 16–33.
- [32] W. Liu, J. Li, M. Cheng, Q. Wang, Y. Qian, K.W.K. Yeung, P.K. Chu, X. Zhang, A surface-engineered polyetheretherketone biomaterial implant with direct and immunoregulatory antibacterial activity against methicillin-resistant *Staphylococcus aureus*, *Biomaterials* 208 (2019) 8–20.
- [33] Y. Lai, Y. Li, H. Cao, J. Long, X. Wang, L. Li, C. Li, Q. Jia, B. Teng, T. Tang, J. Peng, D. Eglin, M. Alini, D.W. Grijpma, G. Richards, L. Qin, Osteogenic magnesium incorporated into PLGA/TCP porous scaffold by 3D printing for repairing challenging bone defect, *Biomaterials* 197 (2019) 207–219.
- [34] R. Ma, Y.X. Lai, L. Li, H.L. Tan, J.L. Wang, Y. Li, T.T. Tang, L. Qin, Bacterial inhibition potential of 3D rapid-prototyped magnesium-based porous composite scaffolds—an in vitro efficacy study, *Sci. Rep.* 5 (2015) 13775.
- [35] J. Jang, J.Y. Park, G. Gao, D.W. Cho, Biomaterials-based 3D cell printing for next-generation therapeutics and diagnostics, *Biomaterials* 156 (2018) 88–106.
- [36] H.W. Kang, S.J. Lee, I.K. Ko, C. Kengla, J.J. Yoo, A. Atala, A 3D bioprinting system to produce human-scale tissue constructs with structural integrity, *Nat. Biotechnol.* 34 (3) (2016) 312–319.
- [37] A. Dobos, J. Van Hoorick, W. Steiger, P. Gruber, M. Markovic, O.G. Andriotis, A. Rohatschek, P. Dubrue, P.J. Thurner, S. Van Vlierberghe, S. Baudis, A. Ovsianikov, Thiol-gelatin-norbornene bioink for laser-based high-definition bioprinting, *Adv Healthc Mater* 9 (15) (2020), e1900752.
- [38] N. Söhling, J. Neijhoft, V. Nienhaus, V. Acker, J. Harbig, F. Menz, J. Ochs, R. D. Verboket, U. Ritz, A. Blaeser, E. Dörsam, J. Frank, I. Marzi, D. Henrich, 3D-printing of hierarchically designed and osteoconductive bone tissue engineering scaffolds, *Materials* 13 (8) (2020).
- [39] S.J. Hollister, Porous scaffold design for tissue engineering, *Nat. Mater.* 4 (7) (2005) 518–524.
- [40] F.E. Freeman, D.C. Browe, J. Nulty, S. Von Eeuw, W.L. Grayson, D.J. Kelly, Biofabrication of multiscale bone extracellular matrix scaffolds for bone tissue engineering, *Eur. Cell. Mater.* 38 (2019) 168–187.
- [41] K. Hölzl, S. Lin, L. Tytgat, S. Van Vlierberghe, L. Gu, A. Ovsianikov, Bioink properties before, during and after 3D bioprinting, *Biofabrication* 8 (3) (2016), 032002.
- [42] Y. Yang, M. Wang, S. Yang, Y. Lin, Q. Zhou, H. Li, T. Tang, Bioprinting of an osteocyte network for biomimetic mineralization, *Biofabrication* 12 (4) (2020), 045013.
- [43] J.B. Mandell, S. Orr, J. Koch, B. Nourie, D. Ma, D.D. Bonar, N. Shah, K.L. Urish, Large variations in clinical antibiotic activity against *Staphylococcus aureus* biofilms of periprosthetic joint infection isolates, *J. Orthop. Res.* 37 (7) (2019) 1604–1609.
- [44] E. Seebach, K.F. Kubatzky, Chronic implant-related bone infections-can immune modulation be a therapeutic strategy? *Front. Immunol.* 10 (2019) 1724.
- [45] E.M. Schwarz, J. Parvizi, T. Gehrke, A. Aiyer, A. Battenberg, S.A. Brown, J. Callaghan, M. Citak, K. Egol, G.E. Garrigues, M. Ghert, K. Goswami, A. Green, S. Hammond, S.L. Kates, A.C. McLaren, M.A. Mont, S. Namdari, W.T. Obrebsky, R. O'Toole, S. Raikin, C. Restrepo, B. Ricciardi, K. Saeed, J. Sanchez-Sotelo, N. Shohat, T. Tan, C.P. Thirukumaran, B. Winters, 2018 international consensus meeting on musculoskeletal infection: research priorities from the general assembly questions, *J. Orthop. Res.* 37 (5) (2019) 997–1006.
- [46] L. Chu, Y. Yang, S. Yang, Q. Fan, Z. Yu, X.L. Hu, T.D. James, X.P. He, T. Tang, Preferential colonization of osteoblasts over co-cultured bacteria on a bifunctional biomaterial surface, *Front. Microbiol.* 9 (2018) 2219.
- [47] Y. Yang, S.B. Yang, Y.G. Wang, S.H. Zhang, Z.F. Yu, T.T. Tang, Bacterial inhibition potential of quaternised chitosan-coated VICRYL absorbable suture: an in vitro and in vivo study, *J. Orthop. Translat.* 8 (2017) 49–61.
- [48] Z.X. Peng, L. Wang, L. Du, S.R. Guo, X.Q. Wang, T.T. Tang, Adjustment of the antibacterial activity and biocompatibility of hydroxypropyltrimethyl ammonium chloride chitosan by varying the degree of substitution of quaternary ammonium, *Carbohydr. Polym.* 81 (2) (2010) 275–283.
- [49] H. Tan, Z. Peng, Q. Li, X. Xu, S. Guo, T. Tang, The use of quaternised chitosan-loaded PMMA to inhibit biofilm formation and downregulate the virulence-associated gene expression of antibiotic-resistant *Staphylococcus*, *Biomaterials* 33 (2) (2012) 365–377.
- [50] D.F. Duarte Campos, M. Rohde, M. Ross, P. Anvari, A. Blaeser, M. Vogt, C. Panfil, G.H. Yam, J.S. Mehta, H. Fischer, P. Walter, M. Fuest, Corneal bioprinting utilizing collagen-based bioinks and primary human keratocytes, *J. Biomed. Mater. Res.* 107 (9) (2019) 1945–1953.
- [51] X. Liu, C. Ji, L. Xu, T. Yu, C. Dong, J. Luo, Hmox1 promotes osteogenic differentiation at the expense of reduced adipogenic differentiation induced by BMP9 in C3H10T1/2 cells, *J. Cell. Biochem.* 119 (7) (2018) 5503–5516.